On the role of droplets in cocurrent annular and churn-annular pipe flow

J.M.C. van 't Westende *, H.K. Kemp, R.J. Belt, L.M. Portela, R.F. Mudde, R.V.A. Oliemans

J.M. Burgerscentrum for Fluid Mechanics, Delft University of Technology, Kramers Laboratorium, Prins Bernhardlaan 6, 2628 BW Delft, The Netherlands

Abstract

Decreasing the gas flow-rate in an initially vertical upward annular dispersed pipe-flow, will eventually lead to a down-flow of liquid. The onset of this down-flow has been related in the literature to the presence of the dispersed phase and the instability of the liquid film. Here we investigate how the dispersed-phase may influence the down-flow, performing detailed PDA-measurements in a 5 cm vertical air–water annular-flow. It is shown that the dispersed-phase does not cause the liquid down-flow, but that it delays the onset of liquid down-flow. In cocurrent annular flow the dispersed phase seems to stabilise the film flow, whereas in churn-annular flow the opposite seems to be true.
© 2007 Elsevier Ltd. All rights reserved.

Keywords: Upward annular flow; Two-phase gas–liquid flow; Droplets; PDA

1. Introduction

A plot of measured pressure losses for vertical annular gas/liquid flow from low to high gas velocities displays a minimum at a densimetric gas Froude number of 1 (Wallis (1969)). Operating conditions between the flooding point and the point of minimum pressure gradient are frequently indicated as churn or churn-annular flow. In the production of natural gas from underground gas wells, liquid (water, oil, condensate) is usually produced simultaneously. The flow pattern inside the production tubing is an annular dispersed two-phase flow: the liquid phase flows partly as a wavy film along the pipe circumference, and partly as entrained droplets in the turbulent gas core. At the end of the lifetime of gas wells, the gas production rate decreases strongly. Due to this decrease, the drag force of the gas phase exerted on the liquid phase might not be sufficient anymore to bring all the liquid to the surface, and liquid starts to drain downward (flow reversal). In such a situation, depending on the gas reservoir conditions (Oudeman (1989)), the liquid could accumulate downhole,

---

* Corresponding author. Tel.: +31 15 278 7084; fax: +31 15 278 2838.
  E-mail address: j.m.c.vantwestende@tudelft.nl (J.M.C. van 't Westende).

block the inflow into the production tubing and gas production could cease. This phenomenon is called liquid loading, occurs at a gas rate below the minimum in the pressure gradient curve, and is closely related to flooding. Its origin is ascribed in the literature to the dispersed-phase or the film flow.

- In the gas producing industry, the onset of liquid loading is commonly predicted using a correlation developed by Turner et al. (1969). The idea behind this correlation is to estimate the minimum gas velocity that can keep the largest droplet, present in the gas core, pending. When the gas velocity in the production tubing gets below this minimum velocity, liquid loading will occur. It is, thus, implicitly assumed that the dispersed phase is causing liquid loading, although direct evidence for this is not available.
- Zabaras et al. (1986) identified a switching behaviour of the wall-shear near flooding conditions (i.e., the wall-shear is alternately directed upwardly and down-wards). Following their idea the onset of liquid loading is coupled to the instability of the liquid film. This instability is influenced by the presence of the dispersed phase, decreasing both the film-thickness and the interfacial friction.

From the above it is clear that there is no consensus on the process of liquid loading, and to what extent the dispersion is responsible. To better understand the role of the dispersion in an annular flow close to liquid loading, we need to know the pdf of the drop-diameter, the pdf of the drop-velocity, the pressure-gradient and the amount of entrainment. Moreover, we want to know the spatial distribution of these dispersed-phase properties.

However, most of the data on the properties of the dispersed phase in an annular flow presented in the literature are obtained with methods that can only measure drop-size distributions, (e.g., photography, immersion method, or laser diffraction). Only a few show simultaneous measurements of drop-sizes and droplet-velocities, (e.g., Phase Doppler Anemometry (PDA), or a laser grating technique). Furthermore, the flow-conditions are mostly cocurrent annular flows, whereas, for our purpose, it is essential to have detailed information of drop-sizes, and droplet-velocities simultaneously near the transition from cocurrent to churn-annular flow, see Table 1.

The objective of this paper is to provide detailed data on the characteristics of the dispersed phase in cocurrent annular flow and churn-annular pipe flow, with the aim to understand to what extent the droplets are contributing to the liquid down-flow transition in the churn-annular region. Experiments have been performed using PDA, providing us with both drop size and drop velocity measurements. Simultaneously, we have measured the total pressure-gradient, the amount of liquid down-flow and the amount of entrainment. In Section 2.1 we briefly discuss some of the general phenomena observed when the flow pattern changes from a cocurrent annular flow to a churn-annular flow. We show the model of Turner et al. (1969) in Section 2.2, and the pressure gradient contribution of the dispersed phase in Section 2.3. In Section 3 we describe the flow loop, and in Section 4 the post-processing of the PDA-data. The results of the measurements, both for the gas phase

Table 1
Flow conditions and measurement techniques used in published studies on annular dispersed pipe flow (not an exhaustive list)

Author	Measurement technique	u_{sg} (m/s)	u_{sl} (cm/s)	D (mm)	d_{32} μm
Azzopardi et al. (1991)	Diffraction	30	4	20	104
Azzopardi and Teixeira (1994)	PDA	20	1.6	32	209
Fore and Dukler (1995b)	Laser-grating	20	1.5	51	462
Hay et al. (1998)	Photography	30	1.4	42	138
Zaidi et al. (1998)	PDA	30	3	38	280
	Diffraction	30	3	38	180
Simmons and Hanratty (2001)	Diffraction	30	2.2	95	116
Al-Sarkhi and Hanratty (2002)	Diffraction	30	4	25	103
Hurlburt and Hanratty (2002)	Immersion	30	4	95	99
		20	7	95	145
Current study	PDA	12	4	50	255
		21	4	50	161

We show here the superficial gas-velocity, u_{sg}, the superficial liquid-velocity, u_{sl}, the pipe diameter, D, and the measured Sauter-mean drop-diameter, d_{32}, reported in those studies.

and the dispersed phase, are presented together with their discussion in Section 5, and concluding remarks are given in Section 6.

2. Phenomena in annular dispersed flows

2.1. Cocurrent to churn-annular flow

When a high-speed air–stream flows through a vertical pipe with diameter $D = 5$ cm, e.g., with a superficial gas velocity, $u_{sg} = 40$ m/s, and liquid is flowing simultaneously through the pipe with moderate speed, e.g., a superficial liquid velocity, $u_{sl} = 4$ cm/s, the flow pattern will be a cocurrent annular dispersed flow.

When we decrease the gas velocity, while keeping the liquid volume flux constant, the slip with the gas–liquid interface decreases, leading to a smaller interfacial shear, and hence the total pressure-gradient, ∇p_{tot}, decreases, Fig. 3. The amount of entrained liquid also decreases as the gas rate declines. Due to the decrease in both interfacial shear and entrainment, the liquid film-thickness increases, and larger roll-waves are present, making the interface more rough (i.e., the interfacial friction factor becomes larger, Lopes and Dukler (1986)).

Upon further decrease of the gas velocity the pressure-gradient and the amount of entrainment reach a minimum. For the air–water system described above, this minimum occurs at $u_{sg} \approx 20$ m/s, corresponding with a densimetric Froude number, $Fr_g = \frac{u_{sg}^2}{gD} \frac{\rho_g}{\rho_l - \rho_g} \approx 1$, where g is the gravitational acceleration, and ρ_g and ρ_l are the density of the gas phase and the liquid phase, respectively.

When decreasing the gas velocity below $Fr_g = 1$, the liquid film thickness and the wave height become much larger. According to Zabaras et al. (1986) the wall-shear is occasionally directed upward, and film-churning occurs. The interfacial shear has to increase to balance the increasing weight of the liquid film, hence the pressure-gradient increases. Note that the amount of entrainment also increases again. A schematic of the flow structure for churn-annular and annular flow, respectively left and right of the pressure gradient minimum, is shown in Fig. 1.

When in the churn-annular regime the gas velocity is further decreased less and less liquid is dragged upwards: the smaller interfacial waves are tumbling cocurrently over the base film, which seems to drain downward. Occasionally, large interfacial waves (highly aerated) are propelled fast with the gas flow; possibly these waves correspond to the huge waves reported by Sekoguchi and Takeishi (1989). Here, the onset of liquid down-flow is referred to as the flow-reversal point, and, in general, occurs at a gas velocity below the minimum in the pressure-gradient curve.

Eventually, upon decreasing the gas flow-rate further below the flooding-point, all liquid flows counter-currently with the gas phase.
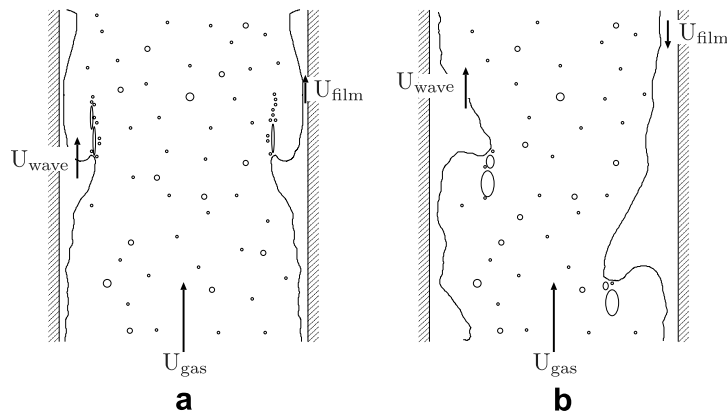

Fig. 1. Schematic cross-section of (a) a cocurrent annular flow and (b) a churn-annular dispersed flow. In churn-annular flow droplets are atomised from upward going flooding waves, the base liquid film drains downward. In cocurrent flow, droplets are formed from disturbance waves; the liquid film is less thick and uni-directional.

The gas velocities of the flow-reversal point and the flooding-point can be quite close together, especially for small liquid flow-rates. This indicates that rather subtle changes, can lead to dramatic differences in the flow.

2.2. Onset of liquid loading, turner criterion

The most widely applied method for predicting the flow-reversal point is based on an analysis of droplet transport in a vertical turbulent gas flow by Turner et al. (1969). They related the onset of liquid loading, with the ability of the gas stream to keep the largest droplet pending.

To estimate the size of the largest droplet present in the turbulent flow, $d_{dr,max}$, they used a correlation involving a critical Weber number. Droplets with a larger diameter are assumed to shatter due to the droplet-gas interactions.

$$We_{crit} = \frac{\rho_g V_{T,dr,max}^2 \, d_{dr,max}}{\sigma} = 30, \tag{1}$$

σ is here the surface tension and $V_{T,dr,max}$ represents the terminal free-fall velocity for the largest drop, and $u_{sg} = V_{T,dr,max}$ is the predicted flow-reversal point gas-velocity.

They assumed that the largest drop still is spherical, and that it has a drag coefficient, $C_D = 0.44$. This results in a correlation for $V_{T,dr,max}$:

$$V_{T,dr,max} = \left(\frac{90.9g\sigma(\rho_l - \rho_g)}{\rho_g^2} \right)^{0.25}. \tag{2}$$

This gives for an air–water system a maximum droplet diameter $d_{dr,max} = 8.5$ mm, with a corresponding terminal free-fall velocity, $V_{T,dr,max} = 14.5$ m/s.

Although for an air–water flow in a 50 mm diameter vertical pipe, Turners correlation seems to give a good prediction of the flow-reversal point, it is not likely that drops with such a large diameter will be present. Maximum drop diameters, reported in the literature for air–water systems, are about 2000 μm, depending on flow rates, systems dimensions and measurement technique used, see, e.g., Azzopardi and Hewitt (1997). The waves producing the droplets are in general much smaller than the estimate of the maximum drop diameter resulting from Eq. (1) and (2). So, in order to generate drops of the size needed for the Turner criterion coalescence has to be very strong. This is unlikely for the relatively dilute conditions at which gas wells operate.

2.3. Dispersed-phase pressure-gradient

When a droplet is created from the gas–liquid interface, its initial velocity is much smaller than the gas velocity. Due to the drag force exerted on the droplet, it will accelerate, increasing its kinetic energy. When the droplet impinges onto the gas–liquid interface, its kinetic energy is converted partly to kinetic energy of the liquid film (pushing the liquid film upward), but mostly to heat (via friction with the wall, according to Lopes and Dukler (1986) and Fore and Dukler (1995a)). The conversion of energy from kinetic to heat makes it no longer available for transporting the liquid phase upward cocurrently with the gas phase, and thus the acceleration of the dispersion can be interpreted as an energy loss, resulting in a dispersed-phase pressure-gradient: the dispersion effectively blocks the gas-flow.

For a constant total pressure-gradient the dispersed-phase pressure-gradient increases for an increasing amount of entrainment. The interfacial shear then has to decrease, which will make the liquid film more unstable. On the other hand, increasing the entrainment also decreases the film flow-rate: the liquid film becomes thinner, making it more stable. The balance of the stabilising and destabilising effects depends on the value of the dispersed-phase pressure-gradient for a given amount of entrainment.

The dispersed-phase pressure-gradient, ∇p_{dr}, can be estimated directly from the PDA-measurements (as we will show below), or indirectly using a model derived by Lopes and Dukler (1986). The indirect method of Lopes and Dukler is a more coarse approach, using the end-result of the acceleration process, i.e., the increase in droplet-momentum; ∇p_{dr} is estimated using a mean droplet axial-velocity at the center of the pipe, and an average rate of atomisation.

2.3.1. Model of Lopes and Dukler

Following a momentum balance Lopes and Dukler obtain:

$$\nabla p_{dr} = \frac{4}{D - 2\delta_f} R_A (u_{z,dep,dr} - u_{z,at,dr}) + \alpha_{dr}\rho_l g, \tag{3}$$

where δ_f is the film thickness, R_A is the rate of atomisation, and $u_{z,dep,dr}$ and $u_{z,at,dr}$ are the droplets axial-velocity just before deposition and just after atomisation, respectively. α_{dr} is the holdup of the dispersed phase, and g is the gravitational acceleration.

The rate of atomisation and the holdup are related via:

$$R_A = \frac{\alpha_{dr}\rho_l(D - 2\delta_f)}{4 t_{res,dr}}, \tag{4}$$

where $t_{res,dr}$ is a characteristic residence time of the droplets, and can be estimated with:

$$t_{res,dr} = D/u_{lat,dr}, \tag{5}$$

where $u_{lat,dr}$ is a characteristic droplet lateral-velocity, i.e., the droplet velocity projected onto the cross-section of the pipe.

Fore and Dukler (1995a) determine R_A indirectly by measuring the rate of deposition, R_D, with a double film-extraction technique, and assuming $R_A = R_D$. $u_{z,dep,dr}$ is estimated with the arithmetic-mean centerline droplet-velocity, which they measured using a laser-grating technique, and $u_{z,at,dr}$ is assumed to be equal to the wave velocity.

3. Flow loop

The flow loop consists of a 50 mm acrylic pipe, placed vertical with a total length of 12 m, Fig. 2. Dry air, supplied by a compressor is blown into the tube at near atmospheric conditions, and at 1 m downstream from the gas inlet a water film is created along the pipe circumference, using a porous wall. Both the air and water flow rates are controlled with rotameters with an accuracy of 2% for the gas flow and 4% for the liquid flow. The superficial air velocity ranges from 10 to 40 m/s, and the superficial water velocity is set at 1, 2, 4 or 8 cm/s.

Pressure drop measurements are performed between 80 and 140 pipe diameters from the liquid inlet using a water manometer with a read-out accuracy of about 10 Pa. For the churn-annular flow conditions, however, the strong pressure fluctuations deteriorate the accuracy down to about 450 Pa. Measuring the pressure gradient in this way, the difference between a single-phase turbulent gas flow and the Blasius curve is below 10%, for 5 m/s < u_{sg} < 50 m/s, see Fig. 3.

PDA measurements are performed at 7.5 m downstream from the liquid inlet (150 tube diameters). To obtain optical access, the liquid film is extracted in two steps: (i) the base film is removed using a porous wall, and (ii) the remaining waves are extracted using a slit. With the slit, the pipe diameter is reduced to 40 mm, and therefore only the droplet-laden gas-core flows through the PDA section; the distance between the slit and the
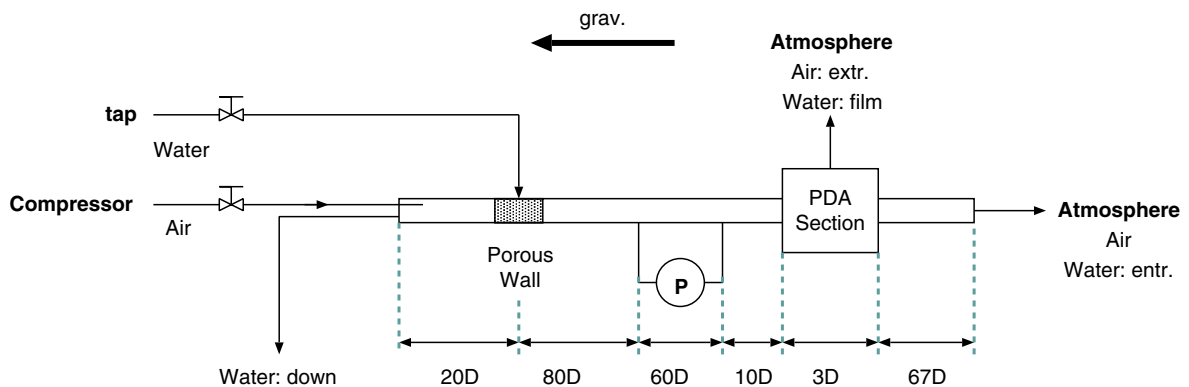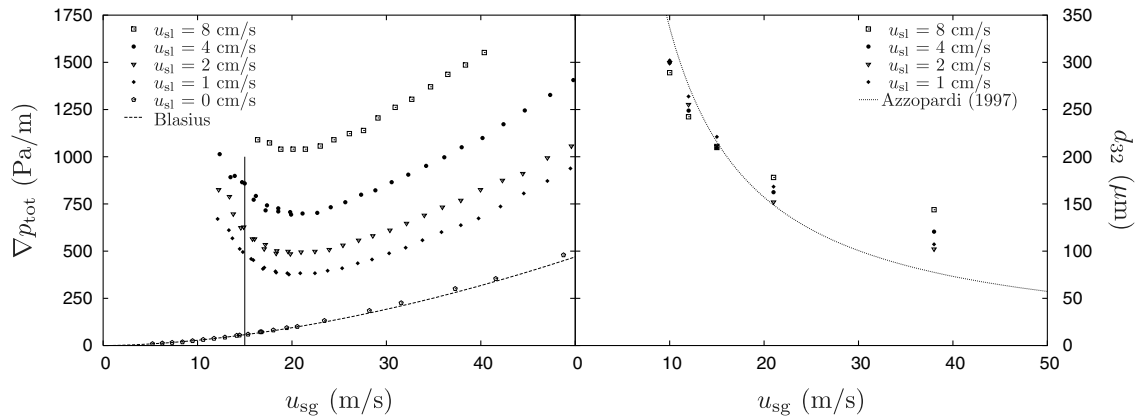

Fig. 2. Flow loop.

Fig. 3. Left: total pressure-gradient in vertical annular flow. At $u_{sg} \approx 15$ m/s liquid starts to flow counter-current with the gas stream, liquid loading (solid line). We did not measure the pressure-gradient down to the flooding point. For comparison, single phase measurements are shown as well together with the pressure gradient prediction of Blasius. Right: measured Sauter-mean diameter in center of pipe. The solid line represents a correlation of the drop size that is found in Azzopardi (1997), ignoring coalescence.

measurement area of the PDA is 5 cm, and the total length of the film extraction section and the PDA section is 15 cm. To compensate for the reduced pipe cross-section, we also extract air at the film extraction section and measure its flux, which should be $\approx 30\%$ of the total air flux.

The PDA transmitting optics used is a Dantec 60X Fiber Flow transmitting optics system combined with a Dantec 60X41 transmitter. To measure two velocity components of the droplets we use a pair of green laser beams (514.5 nm, 15.5 mW) and a pair of blue laser beams (488 nm, 20.5 mW), provided by a Stabilite 2016 water cooled Ar-ion laser (Spectra-Physics). A frequency-shift of 40 MHz using a Bragg-cell is applied. The receiving optics consist of a Dantec 57X10 receiving optics fitted with four 57X08 photo-multipliers, allowing us to measure two velocity components and make two drop-size estimates. The signal of the photo-multipliers is past through a Dantec 58N10 signal processor, estimating for each droplet measured: the arrival time of the droplet, the transit time of the droplet, the axial-component and the lateral-component of the velocity of the droplet and the drop-size. A scattering angle of 70° with parallel polarisation is selected for the PDA-setup. The focus of the lens for both the transmitting and the receiving optics is 600 mm; beam separation at the transmitting optics is 38 mm.

Our PDA has been calibrated by measuring four different sized glass-microspheres with a narrow size-distribution (Whitehouse Scientific, general purpose microspheres: GP0049, GP0116, GP0275 and GP0550) using (i) PDA, (ii) laser diffraction (Mastersizer S particle size analyser, Malvern Instruments), and (iii) photography (PCO sensicam QE mounted on a Zeiss axiovert 200 M optical microscope, ≈ 1.6 pixel/μm). All measurement techniques provide similar results with a variation between them of maximum 10%, see Kemp (2004). Table 2 summarises the resolution, range and reproducibility of the measured droplet properties/quantities for a cocurrent annular and churn-annular flow.

At the end of the pipe the liquid phase is collected and measured, and the air is released to the atmosphere; since the liquid film is already extracted stream upward, we can measure the entrainment via the collected

Table 2
Resolution, measuring range and reproducibility for the droplet properties/quantities measured by the PDA

	Resolution	Range	Reproducibility (%)
Arrival time	4 μs	0–∞[a]s	–
Transit time	0.4 μs	0–100 μs	–
Axial velocity	0.06 m/s	−24 to 73 m/s	2
Lateral velocity	0.02 m/s	−8 to 24 m/s	2
Drop size	1.2 μm	0–780 μm	3

[a] The measurement stops when the inter-arrival time of two subsequent droplets is larger than 30 s. By repeating a measurement 5 times at equal flow conditions, we have estimated the reproducibility using the standard deviation.

water at the end-section. In case of a churn-annular flow, part of the liquid phase flows countercurrent with the gas phase, and is drained and measured at the air-inlet; this drain is closed for the gas-flow using a waterlock.

More details on the flow loop, can be found in Westende et al. (2005).

4. Post-processing of the PDA-data

For any property P_{dr} of the dispersed phase, its flux, $\Phi_{P_{dr}}$, and its concentration, $C_{P_{dr}}$, can be computed as a summation of the contributions of all individual droplets, see also Albrecht et al. (2003):

$$\Phi_{P_{dr}} = \sum \frac{P_{dr}}{A_{det,dr}T}, \tag{6}$$

$$C_{P_{dr}} = \sum \frac{P_{dr}}{A_{det,dr}u_{z,dr}T}, \tag{7}$$

where $A_{det,dr}$ is the detection-volume area of a droplet, $u_{z,dr}$ is the axial component of the droplet-velocity, and T is the total measurement time.

The size of the detection-volume area depends on the drop-size, the droplet direction of movement, and the optical parameters of the PDA. In Westende et al. (2005) it is shown how the detection volume can be computed from the measurements. Since annular flows are strongly uni-directional, we use the axial component of the droplet-velocity, $u_{z,dr}$, for estimating $C_{P_{dr}}$.

The droplet volume-flux measured by the PDA should match the entrainment-flux collected at the outlet of the pipe. In order to achieve this, we introduce a correction factor, F_{cor}, and correct all fluxes and concentrations with this factor.

The dispersed-phase holdup, and pressure-gradient can directly be computed from the PDA-measurements as

$$\alpha_{dr} = \sum \frac{\frac{\pi}{6}d_{dr}^3}{A_{det,dr}u_{z,dr}T}, \tag{8}$$

$$\nabla p_{dr} = \sum \frac{F_{D,z,dr}}{A_{det,dr}u_{z,dr}T}, \tag{9}$$

where d_{dr} is the droplet diameter, and $F_{D,z,dr} = C_D \frac{1}{2}\rho_g u_{z,s,dr}^2 \frac{\pi}{4}d_{dr}^2$ is the drag force acting on a single drop. C_D is the drag coefficient, and $u_{z,s,dr} = u_{z,g} - u_{z,dr}$, is the axial component of the droplet slip-velocity, with $u_{z,g}$ being the gas-phase axial-velocity

The Sauter-mean-diameter is calculated via:

$$d_{32} = \sum \frac{d_{dr}^3}{A_{det,dr}u_{z,dr}T} \bigg/ \sum \frac{d_{dr}^2}{A_{det,dr}u_{z,dr}T} \tag{10}$$

A droplet axial-velocity related to the droplet momentum is the mass-weighted droplet axial-velocity (i.e., it is the total momentum divided by the total mass of the dispersed phase):

$$\bar{u}_{z,dr} = \sum \frac{\rho_l \frac{\pi}{6}d_{dr}^3 u_{z,dr}}{A_{det,dr}u_{z,dr}T} \bigg/ \sum \frac{\rho_l \frac{\pi}{6}d_{dr}^3}{A_{det,dr}u_{z,dr}T}. \tag{11}$$

Since the axial momentum-concentration (numerator of Eq. (11)) can also be viewed as the mass-flux, $\bar{u}_{z,dr}$ also links the droplet volume-flux and the droplet holdup.

From Eqs. (8) and (9) for the dispersed-phase holdup and pressure-gradient, derived from the centerline PDA-data, we have calculated the residence-time using Eqs. (3) and (4).

$$t_{res} = \bar{u}_{z,dr}\left(\frac{\nabla p_{dr}}{\rho_l \alpha_{dr}} - g\right)^{-1}, \tag{12}$$

where we have neglected $u_{z,at,dr}$ in Eq. (3), and assumed $u_{z,dep,dr} = \bar{u}_{z,dr}$ at $y = 0$.

5. Measurement results

In the left graph of Fig. 3 we show the total pressure-gradient for four different values of u_{sl} as a function of u_{sg}. The measurements of a single-phase gas-flow, and the corresponding prediction using Blasius correlation for the friction factor are plotted here as well. The vertical solid line represents roughly the gas-phase velocity at which flow-reversal starts. With the single-phase flow we observe a 5% overestimation of the Blasius correlation for $u_{sg} < 25$ m/s, and about 8% for larger gas flow-rates. For the two-phase flows we see that the pressure-gradient is much larger than the single phase, even with small liquid flow-rates. For all liquid flow-rates we observe a minimum in the pressure-gradient at about $u_{sg} = 20$ m/s, corresponding to $Fr_g = 1$, see also Zabaras et al. (1986).

In the right graph of Fig. 3 the measured Sauter-mean droplet-diameter is plotted, together with a correlation given by Azzopardi (1997):

$$\frac{d_{32}}{D} = 1.91 Re_{sg}^{0.1} We_{sg}^{-0.6} (\rho_g/\rho_l)^{0.6} + 0.4 E u_{sl}/u_{sg}, \tag{13}$$

where $Re_{sg} = \rho_g u_{sg} D/\mu_g$ is the gas-phase Reynolds number, and $We_{sg} = \rho_g u_{sg}^2 D/\sigma$ is the gas-phase Weber number. μ_g is the gas-phase dynamic-viscosity, and E is the amount of entrainment. The second term in the RHS of Eq. (13) is the contribution from drop coalescence.

For $u_{sg} > 20$ m/s the correlation underpredicts our measured values for d_{32}. We observe an increase of d_{32} with increasing u_{sl}, probably due to increasing coalescence. Here we note that including the coalescence term with $E = 1$ will result in an increase of d_{32} of about 20 μm for $u_{sg} = 40$ m/s and $u_{sl} = 8$ cm/s. It is interesting to observe that the correlation of Azzopardi (1997) approximates the drop size fairly well in the churn-annular regime, indicating that there may be similar atomisation mechanisms in both churn-annular and cocurrent annular flow. We see that increasing the liquid flow-rate slightly decreases d_{32}. For all gas flow-rates we see that the measurements with $u_{sl} = 1$ cm/s behave unexpectedly, i.e., they do not show the smallest value for d_{32}.

In order to study the transition of cocurrent to churn-annular flow, we show some flow-details in the following sections for two gas flow-rates: one just above the minimum in the pressure-gradient curve, $u_{sg} = 21$ m/s, and the other in between the flooding point and the flow-reversal point, $u_{sg} = 12$ m/s. In Table 3 we show some characteristic flow parameters for the flow conditions we have measured. For comparison, also the results

Table 3
Mean parameters measured in the churn-annular flows and the cocurrent annular flows

	Current study						Fore and Dukler (1995a,b)		
Name	G12L1	G12L2	G12L4	G21L1	G21L2	G21L4	FD1	FD2	FD3
u_{sg} (m/s)	12.1	12.1	12.2	21.3	21.4	21.2	20.2	20.2	20.1
u_{sl} (cm/s)	0.97	1.97	3.94	0.94	2.01	4.11	1.5	3	4.5
∇p_{tot} (Pa/m)	670	825	1015	385	500	700	476	517	657
$u_{\nabla p}$ (m/s)	2.6	2.9	3.3	2.0	2.3	2.7	2.2	2.3	2.6
E	0.58	0.46	0.40	0.11	0.32	0.43	0.23	0.30	0.32
$\Phi_{l,down}$ (%)	11	3	7	0	0	0			
δ_f (μm)	1015	1171	1358	335	428	565	454	499	584
d_{32} (μm)	265	261	255	172	157	161	462	533	668
$u_{z,dep,dr}$ (m/s)	12.3	13.0	13.5	22.9	24.1	24.7	22.7	23.2	23.5
$u_{z,at,dr}$ (m/s)	0.0	0.3	2.1	1.1	1.4	1.6	1.30	1.45	1.45
$u_{z,s,dr}$ (m/s)	5.3	5.6	5.7	7.3	5.7	4.5			
C (mm^{-3})	0.19	0.30	0.52	0.08	0.56	1.17			
α_{dr} (10^{-4} m^3/m^3)	5.1	8.0	13.6	0.51	3.0	7.9	2.1	5.6	8.9
t_{res} (s)	0.22	0.20	0.15	0.14	0.17	0.23			
R_A (g/m^{2}s)	28	49	105	4.6	21	41	12.4	23.5	25.6
$L_{z,dr}/D$	56	50	39	59	75	100			
∇p_{dr} (Pa/m)	31	54	98	8	37	76	23	47	54

E is the amount of entrainment, $\Phi_{l,down}$ is the liquid down flow, C is the droplet concentration, and $L_{z,dr}$ is the axial distance covered by the droplets, and is computed as $L_{z,dr} = \bar{u}_{z,dr} t_{res,dr}$. For comparison we also show the measurements of Fore and Dukler (1995a), FD1–FD3. The film-thickness and the wave-velocity, i.e., $u_{z,at,dr}$, are measured with a similar technique as done by Fore and Dukler.

measured by Fore and Dukler (1995a,b) for $u_{sg} = 20$ m/s are given. We present here only the details for $u_{sl} = 1$, 2, or 4 cm/s, since these compare best with the results of Fore and Dukler. Most of the data in Table 3 for the condition G21L2 compare favourably with the interpolated Fore and Dukler conditions FD1 and FD2. The drop size d_{32} is an exception: our measurement of $d_{32} = 157$ μm is much smaller than the value of 485 μm from the interpolation. As already clear from the data in Table 1 the laser grating technique used by Fore and Dukler seems to have had a bias to large drop sizes. Such a large drop size is also completely out of line with the literature correlation plotted in Fig. 3.

For each flow condition, we measured at 19 locations in the cross-section of the pipe, in the range $-0.8R < y < 0.8R$, where y is the Cartesian measurement position and R is the pipe radius; on average 10^5 droplets were measured at each position.

In the following sections we present the results of the measured gas-phase velocity profiles (5.1), the drop size distributions (5.2), the drop velocity (5.3), the residence time of the droplets (5.4), and the dispersed phase pressure-gradient (5.5). In Section 5.6 we discuss the consequences of the results for the flow-reversal phenomenon.

5.1. Gas-phase velocity-profiles

We have measured the gas-velocity using 'tracer'-droplets: droplets in the size range: 10 μm $< d_{dr} <$ 20 μm. The relaxation-time, τ_{dr}, of the tracer–droplets is smaller than or of the same order of the time-scale of the large-scale turbulence structures, $\mathcal{T}$, see Table 4. Therefore, the tracer–droplets are expected to follow the mean gas-velocity, and to provide an estimate of the gas-phase turbulence intensity. Droplets with a drop-size smaller than 10 μm are scarce (about 200 on a total droplet-population of 10^5), and they have a very small detection-volume (minimum detectable drop size: $d_{min} \approx 5$ μm), making velocity-estimation from those drops less accurate. Therefore, the droplets smaller than 10 μm are not used for estimating the gas-velocity. The drop-size range for the tracer–droplets extends to 20 μm in order to have enough tracer–droplets to estimate the gas-phase velocity (about 3000 tracer–droplets on a total droplet-population of 10^5). An additional advantage of using droplets as tracers is that they are already present in the flow.

The mean gas-velocity and the gas-velocity fluctuation are shown in Figs. 4 and 5, respectively. For a radial position $|y| > 0.7R$ the gas velocity decays rapidly to zero, which is an indication that, in this region, the flow is disturbed by the film extraction: a new boundary layer has developed. Therefore, we show only results for $|y| \leqslant 0.7R$. For comparison the profiles from a standard large eddy simulation (LES) single-phase pipe-flow are plotted as well: we show the LES-results of a pipe-flow for G21 with a smooth wall (solid line), and with a uniform wall-roughness, $k_s/D = 0.03$ (dashed line), see Westende et al. (2004). Using this hydraulic roughness results in a film thickness of $\delta_f \approx \frac{1}{4}k_s = 375$ μm (Wallis (1969)), which is a reasonable estimate for the film-thickness for G21L1 (see Table 3).

5.1.1. Mean gas-phase velocity

In Fig. 4 we observe that the mean-velocity profiles of G21 are more core-peaked than the LES with a smooth wall, they are roughly similar to the LES with the uniform wall-roughness. The core-peaking is slightly increasing with increasing u_{sl}. This supports the idea that increasing u_{sl} increases the effective roughness of the interface.

Table 4
Characteristic time-scales in annular flows

$\mathcal{T}_{G21L1} = \mathcal{L}/u_{\nabla p,G21L1}$	2.5 ms
$\mathcal{T}_{G12L4} = \mathcal{L}/u_{\nabla p,G12L4}$	1.5 ms
$\tau_{dr,10\ \mu m}$	0.3 ms
$\tau_{dr,20\ \mu m}$	1.2 ms
$\tau_{dr,50\ \mu m}$	7.7 ms
$\tau_{dr,200\ \mu m}$	124 ms

The time scale of the large scale structures are estimated using their length scale, $\mathcal{L} \approx D/10$, and an effective friction-velocity, $u_{\nabla p}$, see Eq. (14).
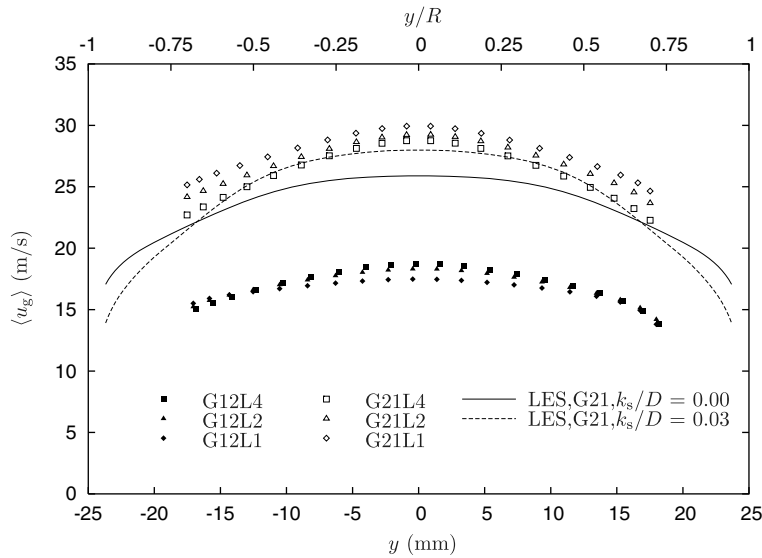
Fig. 4. Profiles of the mean gas-phase velocity for G12L1–G21L4, measured using 'tracer–drops'. The results of a standard LES pipe-flow corresponding to $u_{sg} = 21$ m/s with a smooth wall (solid line), and with a uniform wall-roughness, $k_s/D = 0.03$, (dashed line) are shown.
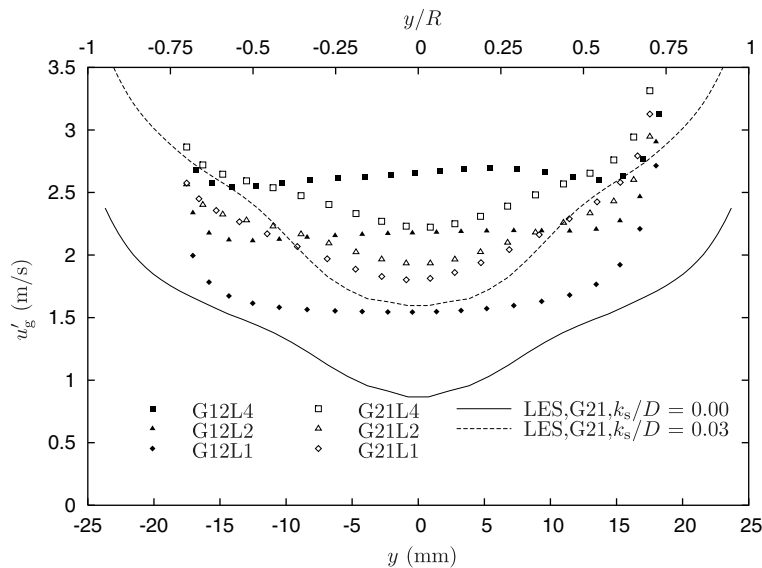

Fig. 5. Profiles of the gas-phase velocity-fluctuation for G12L1–G21L4, measured using 'tracer–drops'. The result of a standard LES pipe-flow with a smooth wall (solid line) or with a uniform wall-roughness, $k_s/D = 0.03$ (dashed line) is shown, corresponding to $u_{sg} = 21$ m/s, Westende et al. (2004).

However, the value of the mean gas-velocity measured with the PDA is about 10% larger than the LES with the uniform roughness. Probably this mismatch is caused by the film extraction section: in order to compensate for reducing the pipe-diameter in this section, gas is extracted simultaneously with the liquid film. In case of, e.g., flow condition G21L1 about 17% of the total gas flow is extracted at the extraction section (see Table 3) whereas about 24% should have been extracted, based on the LES mean velocity-profile with the uniform wall-roughness. This results in a gas-velocity increase of $(1 - \frac{1-0.24}{1-0.17}) \cdot 100\% \approx 8\%$, which is close to the bulk-velocity deviation observed. The resulting acceleration of the gas-phase is probably strongest at larger radial positions, thus flattening the gas velocity-profile. Since, the time it takes for a droplet to cover the distance between the

film extraction and the detection volume is about 2.5 ms (assuming $u_{z,\text{dr}} = 20$ m/s), only the tracer–droplets are affected by a possible distortion of the film-extraction ($\tau_{\text{dr},20\,\mu\text{m}} < 2.5$ ms).

The mean-velocity profile for the churn-annular flows is about 35% lower than for the cocurrent annular flows. The quotient, $\langle u_{\text{g,G21}} \rangle / \langle u_{\text{g,G12}} \rangle$ is constant in the cross-section of the pipe.

5.1.2. Gas-phase velocity fluctuation

The measured axial-velocity fluctuation of the gas-phase in the cocurrent flow conditions is similar to the LES with uniform roughness: it shows a minimum in the center region, although not as low as in the LES. Compared to the LES the turbulence-intensity seems to be enhanced in the center of the flow, possibly by the dispersed phase. The magnitude of the velocity-fluctuation of the measurements are in reasonable agreement with the LES with uniform roughness. Increasing u_{sl} increases the velocity fluctuations. The axial-velocity fluctuations in the churn-annular flow show a different behaviour: the fluctuations are nearly constant in the cross-section of the pipe, and are slightly core-peaking for large u_{sl}. Moreover, the magnitude of the velocity fluctuations is of the same order as those for the cocurrent flow, whereas the bulk-velocity of the churn-annular flows is approximately half the value of the cocurrent flows. Also, the magnitude of the velocity fluctuations depends much stronger on u_{sl}, than in the case of a cocurrent annular flow.

For both the churn-annular flow and the cocurrent annular flow the gas-phase velocity fluctuation scale approximately with the friction velocity, $u_{\nabla p}$, just like in single-phase pipe-flows, see also Table 3. Here we estimate the effective friction velocity via:

$$u_{\nabla p} = \sqrt{\frac{D}{4\rho_{\text{g}}} \nabla p_{\text{tot}}}. \tag{14}$$

Summarising, it seems that a cocurrent annular flow can be described as a single-phase turbulent pipe-flow with wall-roughness. With increasing u_{sl} the effect of the rough interface becomes stronger. Although we find a constant value for the ratio $\langle u_{\text{g,G21}} \rangle / \langle u_{\text{g,G12}} \rangle$, the gas-phase velocity fluctuations of the churn-annular flows behave differently than those of the cocurrent annular flows, and thus we can not describe a churn-annular flow as a single-phase turbulent pipe-flow. The cause of the different behaviour of the churn-annular flow is not yet understood by the authors, but lies probably in the different wave behaviour of the gas–liquid interface.

5.2. Drop size distributions

In Fig. 6 we show the scaled drop-size distributions of the cocurrent annular flows G21L1 and G21L4, and of the churn-annular flow G12L4, at $y = 0$ (solid line; center) and at $y = -0.7R$ (symbols; closest to the receiver, and the smallest path-length of laser light through dispersion).

All distributions show an exponential tail at large drop sizes, and a 'fall-off' at small drop sizes, $d_{\text{dr}} \lesssim 35\,\mu\text{m}$. In the literature a number of possibilities are proposed to predict the drop size distribution, although most of them lack a sound physical background, e.g., the Rosin–Rammler distribution or the upper-limit log-normal (ULLN) distribution, Mugele and Evans (1951). The ULLN gives in general a better fit to the distribution, Simmons and Hanratty (2001). With respect to this, an interesting study is done by Marmottant and Villermaux (2004), who performed experiments on the creation of droplets from a water jet by an air shear-flow. They state that the drop-size distribution is the result of a multiple breakup-coalescence process of the ligaments directly after their creation, resulting in a gamma-distribution, where the initial size of the ligaments determines the tail of the distribution.

An interesting feature of our measurements is that the drop size distribution seems to be the sum of two distributions, since there are two exponential tails. Especially for the cocurrent flows this effect is most clear (see, e.g., G21L1 for which the tails of the two exponential-distributions are indicated with dotted lines). Assuming that droplet breakup and coalescence are not dominant in the core of the flow (see below), this suggests that two independent atomisation processes are occurring simultaneously. Following the idea of Marmottant, a possible explanation is that two types of liquid lumps are created from the waves at the liquid film, each with its own characteristic size. When both lumps break up into droplets via the same process, this
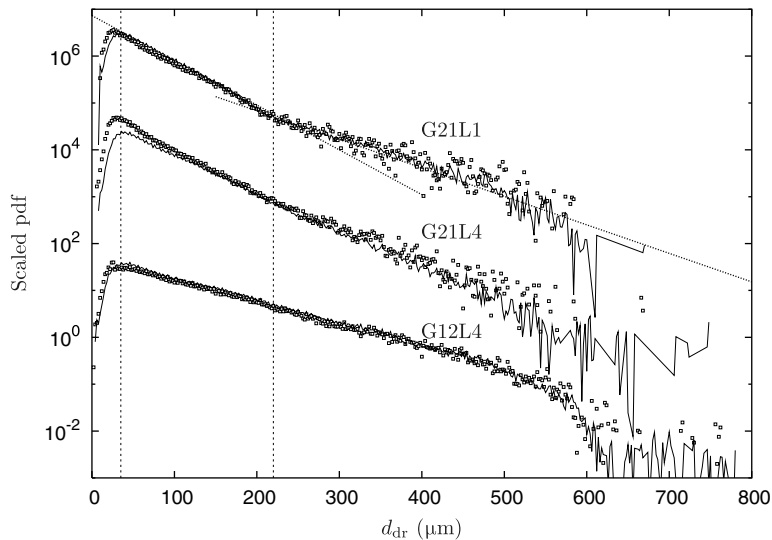
Fig. 6. Drop-size distribution for flow conditions: G21L1, G21L4 and G12L4. The distributions are scaled to optimise the comparison of their shape between different flow conditions and spatial positions. The distributions are corrected for detection-volume dependency and velocity bias. The solid lines correspond to the measurements at $y = 0$, and the symbols to the measurements at $y = -0.7R$. The dashed lines show the approximate position below which the pdf falls to zero, $d_{dr} \approx 35$ μm, and the position of the deflection point of the distribution, $d_{dr} \approx 220$ μm. The dotted lines represent two exponential fits to the tails of the distribution of G21L1.

results in two independent, but similar, distributions, both with their specific exponential tail. We can think of, e.g., bag breakup and ligament breakup providing the different liquid lumps.

For the cocurrent annular flows, we observe that, closer to the gas–liquid interface there are more smaller droplets present (compare, e.g., the solid line with the symbols for G21L4 in the region $d_{dr} < 50$ μm). Comparing the distribution of G21L1 with G21L4, we see that with decreasing u_{sl} this effect disappears. In the churn-annular flows this effect seems absent. Possibly, this is related to the turbophoresis effect, which tends to push the smaller droplets toward the interface. Since the turbophoresis effect scales with the gradient of the turbulence intensity, we speculate that turbophoresis is present in the cocurrent annular flows, increasing with increasing u_{sl}, and that it is absent in the churn-annular flows, see Fig. 5. However, this can only explain the effects for $d_{dr} \lessgtr 25$ μm, for which the relaxation time is of the same order of magnitude as the time-scale of the large-scale turbulence, see Table 4.

5.2.1. Breakup and coalescence

For churn-annular flow we observe a cut-off for $d_{dr} \lessgtr 600$ μm at the pipe centerline, which might be caused by (i) the limited number of droplets in the sample, or (ii) the non-sphericity of the larger drops. On average, only 0.1% of all droplets in churn-annular flow, is larger than 600 μm, making the drop-size distribution very noisy for $d_{dr} > 600$ μm, and a possible cut-off difficult to determine. Since the PDA accepts only spherical droplets (sphericity validation is set to 10%), larger drops that are less difficult to deform have a smaller chance to be measured (e.g., Hay et al. (1998) measured a non-spherical droplet with $d_{dr} = 750$ μm using photography). Since we expect deformation of the droplets to occur earlier than breakup, and since we can not detect deformed droplets, it is likely that the cut-off is related to droplet deformation rather than to droplet breakup. Here we note that maximum drop-sizes reported in literature are about 1 mm and larger, which is well out of our measurement range.

Since the droplets are on average smaller in cocurrent annular flow than those in churn-annular flow, and since the turbulence intensity is of the same order, we expect droplet breakup in the core to be of even less importance for the cocurrent annular flows.

To determine whether coalescence is of any importance, in Fig. 7 we plot the mean free-path-length of the droplets, λ_{dr}, given by:
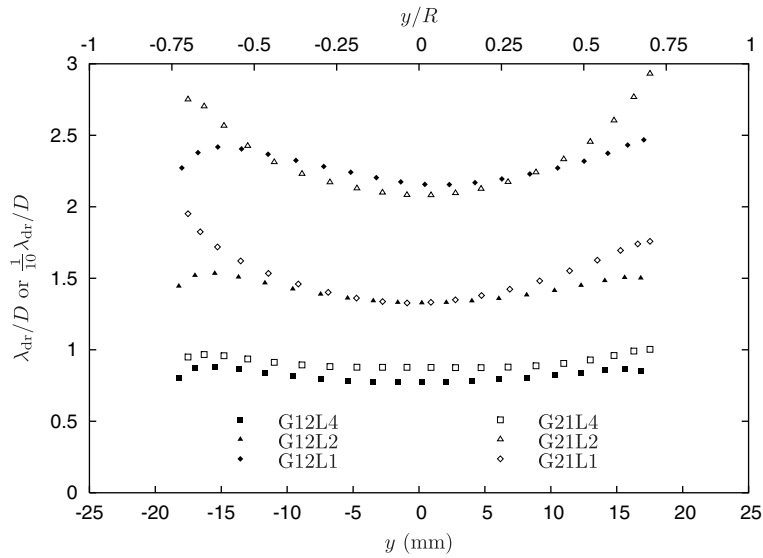
Fig. 7. Droplet mean free-path-length normalised with the pipe diameter. For visualisation reasons we plotted $0.1\lambda_{\mathrm{dr}}/D$ for G21L1.

$$\lambda_{\mathrm{dr}} = \beta_\lambda / C_{A_{\mathrm{dr}}}, \tag{15}$$

where the constant β_λ depends on the details of the drop-size distribution, e.g., for an exponential distribution it can be easily shown that $\beta_\lambda = 3$. $C_{A_{\mathrm{dr}}}$ is the droplet frontal-area concentration.

From Fig. 7 we observe that the free-path-length of the droplets is of the same order of magnitude as the pipe diameter, except for G21L1: $\lambda_{\mathrm{dr,G21L1}} \approx 15D$. For $u_{\mathrm{sl}} = 4$ cm/s, the free-path-length is smaller than the pipe diameter, suggesting that coalescence only starts to influence the dispersion at this liquid flow-rate. As expected, increasing u_{sl} decreases λ_{dr}, due to the increase in droplet concentration; coalescence may become a more dominant process for $u_{\mathrm{sl}} > 4$ cm/s.

From the above it seems that the presented distributions are not affected by breakup or coalescence in the core of the flow. The distribution at a specific location is then a result of the atomisation at the gas–liquid interface and the droplet dispersion. This is also supported by the fact that the tails of the drop size distribution are similar for $y \lessapprox 0.4R$. The droplets in the tails, $d_{\mathrm{dr}} \gtrapprox 100$ μm, all move ballistically.

5.3. Droplet velocity

In Fig. 8 is shown the joint pdf of the droplet diameter and the droplet axial-velocity of G21L2 and G12L2, at $y = 0$ and at $y = -0.7R$, together with the mean axial-velocity of the droplets (solid lines). For G21L2, an estimate of the axial-velocity that a droplet has obtained when it reaches the centerline is plotted as well (dashed lines in the top left graph), with $t_{\mathrm{res}} = 0.02$ s, 0.50 s and t_∞ (terminal velocity); the line with $t_{\mathrm{res}} = 0.02$ s and $t_{\mathrm{res}} = 0.50$ s match approximately the border of the joint-pdf, suggesting 0.02 s $\lessapprox t_{\mathrm{res}} \lessapprox 0.50$ s for G21L2. The joint pdf of the churn-annular flows and the cocurrent annular flows with different u_{sl} are similar, and therefore not shown here.

Since there exists a spread in the residence time of the droplets, see 5.4, and since the droplets are accelerating due to drag from an initially small axial-velocity (approximately the wave-velocity), we expect (i) a spread in the droplet axial-velocity, (ii) the droplet axial-velocity to be skewed to high velocities, and (iii) lots of droplets to have a slip velocity much larger than the terminal free-fall velocity in a stagnant medium, see Fig. 8.

5.3.1. Spread in axial-velocity

A measure for the spread in the droplet axial-velocity is the standard deviation, $u'_{z,\mathrm{dr}}$, which is shown in Fig. 9 for G21L2 and G12L2 in the center of the pipe. In this figure we observe a maximum of $u'_{z,\mathrm{dr}}$ at
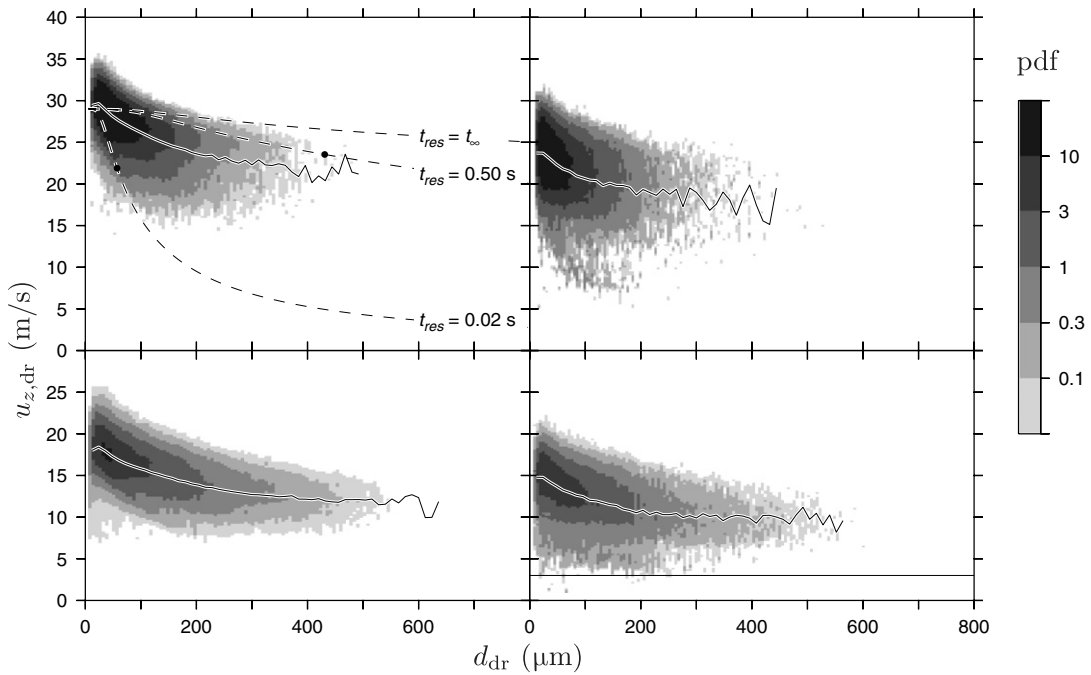
Fig. 8. Scaled joint PDFs of drop size and axial drop velocity of G21L2 (top) and G12L2 (bottom), at $y = 0$ (left) and $y = -0.7R$ (right), together with the mean axial-velocity of the droplets (solid lines). The dashed lines in the top left graph represents the velocity a droplet has obtained when it reaches the center of the pipe (i.e., when it is entrained for $t = \frac{1}{2} t_{res}$); the droplet is accelerated from stand-still in the mean gas-velocity profile of the LES with uniform roughness, while gravity is opposing the drag force ($C_D = 24/Re_{dr} + 0.44$, where Re_{dr} is the droplet Reynolds-number based on the droplet slip-velocity and drop diameter). The symbols plotted on these lines are for the drop sizes with $\tau_{dr} = t_{res}$. In the bottom right graph is also plotted a solid line corresponding to $u_{z,dr} = 3$ m/s.
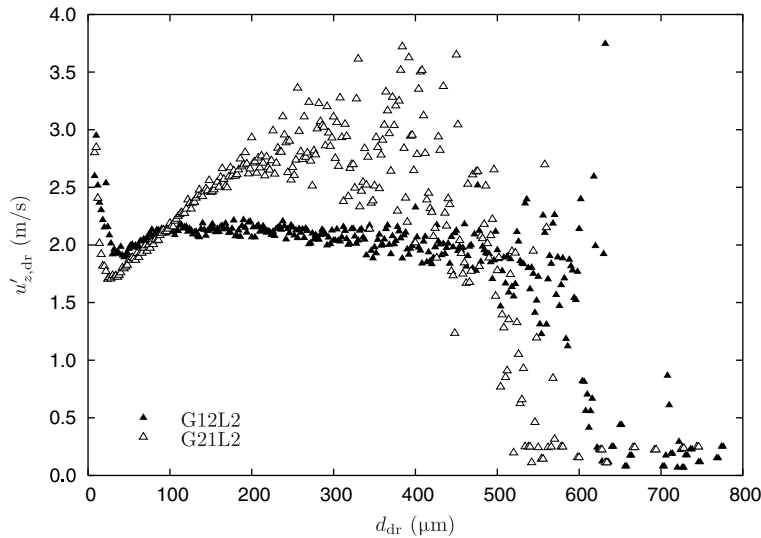

Fig. 9. Standard deviation of droplet axial-velocity for G12L2 and G21L2 in the center of the pipe.

$d_{dr} = 0$, and at $d_{dr} \approx 300$ μm for G21L2; it is unclear why we do not observe a second maximum at larger drop-sizes for G12L2. A minimum is found for $d_{dr} \approx 20$ μm. From this we conclude that the spread in droplet axial-velocity, as caused by the spread in t_{res}, depends on the relaxation time of the droplets, and we expect this velocity spread to be maximum for $\tau_{dr} \approx t_{res,dr}$, with $t_{res,dr}$ a characteristic residence time for the droplets (most clear for G21L2).

Besides this, turbulence affects the smallest droplets ($d_{dr} \lesssim 25\ \mu m$), and results in the increase of $u'_{z,dr}$ with decreasing d_{dr} in this drop-size range.

Azzopardi and Teixeira (1994) also mention the importance of the spread in residence time of the drops to explain the drop-velocity fluctuation. They state that the spread in residence time is caused by the gas turbulence, accelerating and decelerating the smaller drops in the lateral direction. The smaller drops will then have a larger spread in life time, and, according to them, also a larger spread in axial velocities.

However, their suggestion for the velocity spread can not explain the maximum in $u'_{z,dr}$ that is observed. Moreover, for the droplets that feel the gas-phase turbulence (accelerating and decelerating in the lateral direction), the velocity spread in the center of the pipe is most likely linked to the turbulence intensity itself. The joint pdf at $y = 0.7R$ shows a much larger velocity spread than that in the center of the pipe, especially for G21L2. Since the pdf consists of droplets that are recently created and droplets that are about to deposit, the spread in residence time is expected to be larger, hence the spread in velocity is larger.

5.3.2. Skewed axial-velocity distribution

On average, the strength of the acceleration of the droplets decreases during their lifetime. Consequently, the droplet axial-velocity is skewed toward the larger velocities, i.e., it has a negative skewness. This is also observed in the droplet velocity pdf presented by Fore and Dukler (1995b) and Azzopardi (1999). However, here we note that they show the velocity pdf for the dispersion as a whole, which is more skewed due to the variation in drop sizes. For the flow conditions we have measured the skewness is roughly constant with increasing drop size, and has a value of about -0.2 for G12L2 and -0.8 for G21L2. Both Fore and Dukler (1995b) and Azzopardi (1999) also show the existence of droplets with a very large axial-velocity ($u_{z,dr} \approx 1.4u_{sg}$), which is also the case in our flow conditions for $d_{dr} < 100\ \mu m$. The size of these overshoots is about twice the gas-phase velocity-fluctuation as given in Fig. 5, and is probably linked to the most energetic turbulent structures in the flow.

5.3.3. Large axial slip-velocity

From the top left graph of Fig. 8, we see that most of the droplets have a slip velocity much larger than their terminal slip-velocity in a stagnant medium (solid line with $t_{res} = t_{\infty}$); they are still accelerating, hence their slip velocity depends strongly on both the residence time and the drop size.

In Fig. 10 we have plotted the mean droplet slip-velocity, defined as: $\langle u_{z,s,dr} \rangle = \langle u_{z,g} \rangle - \bar{u}_{z,dr}$; using this definition the contribution of the larger droplets has a stronger weight. As a consequence, the slip velocity
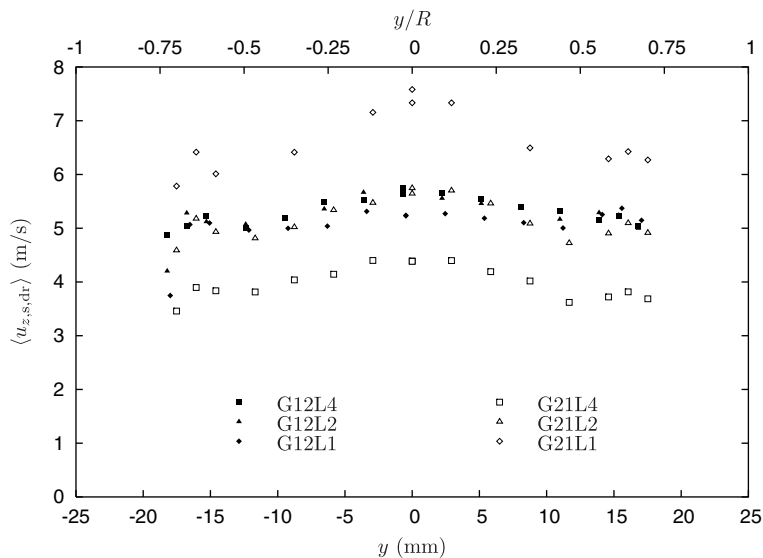

Fig. 10. Droplet slip velocity in cross-section of the pipe.

increases toward the center of the pipe, i.e., the gas-phase velocity increases more strongly toward the center of the pipe than the mass-weighted velocity of the droplets.

For the cocurrent flow conditions we see a strong dependency on u_{sl}, which is absent in the churn-annular flows. Probably, this is a result of the droplet residence-time, which also depends on u_{sl} in the cocurrent-flow, but not in the churn-annular flow, see Section 5.4. An increase of the residence-time decreases the slip-velocity.

Since the slip-velocity is very large, the presence of the droplets will affect the pressure-gradient (see 5.5) and/or the turbulence of the gas-phase, see Fig. 5. From an order of magnitude analysis, Hetsroni (1989) suggested that droplets with $Re_{dr} \gtrsim 400$ tend to enhance turbulence. However, at the center of the pipe, only about 0.1% of the droplets have $Re_{dr} > 400$, whereas about 80% of the droplets have $Re_{dr} < 50$; for the latter group Tsuji et al. (1984) showed that it diminishes turbulence (see Azzopardi (1999)).

5.3.4. Lateral velocity

In Fig. 11 we show the joint pdf of drop size and droplet lateral-velocity for G21L2 in the center of the pipe. From this it is clear that the maximum lateral velocity decreases with increasing drop size, suggesting that the minimum residence-time increases with increasing drop size ($1/t_{res,min} \propto u_{lat,dr,max}$). Because in Fig. 8 the dashed line with $t_{res} = 0.50$ s follows roughly the upper boundary, the maximum residence-time is roughly equal for all drop sizes, and thus we expect the mean residence time to increase with increasing drop size, see also Fig. 13.
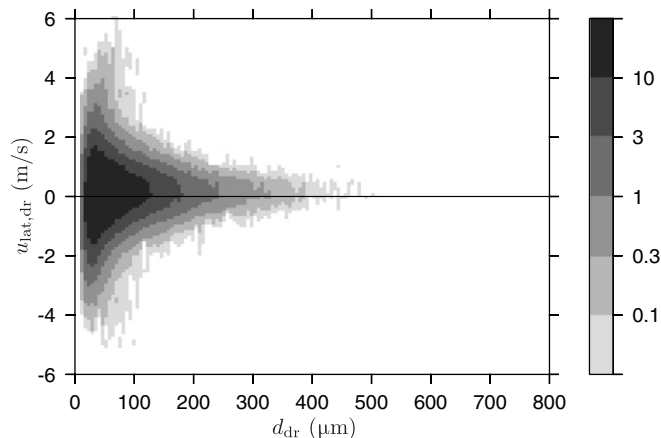

Fig. 11. Joint pdf of drop-size and droplet lateral-velocity for G21L2 in the center of the pipe.
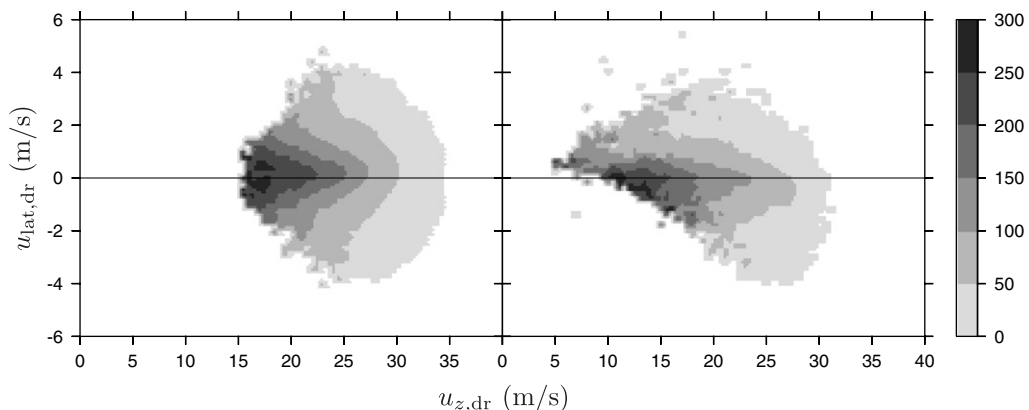

Fig. 12. Volume-averaged volume-mean-diameter for G21L2 at $y = 0$ (left), and at $y = -0.7R$ (right). Positive values of $u_{lat,dr}$ at $y = -0.7R$, represent droplets moving toward the center, and negative values of $u_{lat,dr}$ those moving toward the interface. In the center of the pipe all droplets move toward the interface.
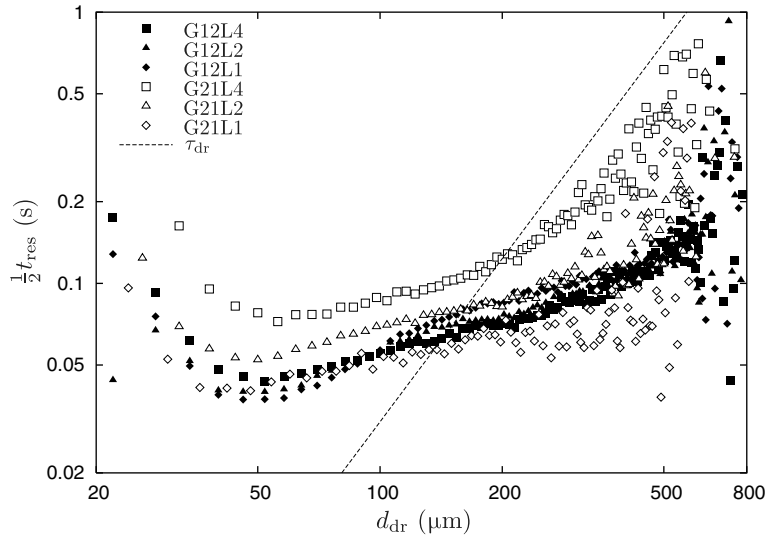
Fig. 13. The time in which a droplet can reach the centerline of the pipe, $\frac{1}{2}t_{\mathrm{res,dr}}$, is plotted versus the drop-size. For comparison the relaxation time is shown as well (dashed line).

In Fig. 12 we show the mean drop-size for a given value for the droplet axial-velocity and lateral-velocity. Smaller droplets have in general a larger lateral-velocity, see Fig. 11, thus we see that in the center of the pipe (left graph) the mean drop-size decreases with increasing lateral-velocity. Also, a smaller droplet will accelerate faster, obtaining larger axial-velocities; this is observed in the center of the pipe as well: an increase in axial-velocity decreases the mean drop-size. Furthermore, since a decrease in lateral velocity results in an increase in the residence-time, we see that for a given mean drop-size the axial-velocity increases with decreasing lateral-velocity (i.e., the droplets have accelerated longer).

Closer to the interface at $y = -0.7R$ (right graph), we see that the symmetry is lost: there is a large difference between (i) the 'young' droplets that are recently entrained, moving toward the center of the pipe ($u_{\mathrm{lat,dr}} > 0$), and (ii) the 'old' droplets that already have crossed the pipe cross-section and move toward the interface ($u_{\mathrm{lat,dr}} < 0$). The old droplets have accelerated for a much longer time-span, and have therefore in general a larger axial-velocity. The young droplets are accelerating more strongly, hence for a given mean drop-size an increase of the lateral-velocity (i.e., a decrease of the residence-time) results in a strong decrease in the axial-velocity.

5.4. Residence time

With the PDA we can not measure the residence-time of an individual droplet directly. However, we need the residence-time to determine R_A (Eq. (4)), or to make a prediction of the droplet axial-velocity, both of which are determining ∇p_{dr}.

Assuming that the droplets move ballistically, the droplet lateral-velocity is well correlated with the droplet residence-time, Eq. (5). Because there exists a large variation in the droplet lateral-velocity (both magnitude and direction), the droplet residence-time is spread as well. With our PDA we can only measure one component of the droplet lateral-velocity, hence we can not use it for computing the residence-time.

Instead, we use Eqs. (3) and (4) to calculate the residence-time from the centerline pressure-gradient (Eq. (9)). In Fig. 13 we show the results of $\frac{1}{2}t_{\mathrm{res,dr}}$ (i.e., the time in which a droplet can reach the centerline of the pipe), computed with Eq. (12). Also, we plot the Stokes relaxation time of the droplets (dashed line).

We observe that for $d_{\mathrm{dr}} \lesssim 40\ \mu\mathrm{m}$ the residence-time increases with decreasing drop-size, because smaller droplets behave more like tracers. Since the gas-phase radial-velocity is zero at the gas–liquid interface, tracers remain, in principle, forever in the gas-stream. The tracer–droplets we use are not ideal tracers, hence they have a finite residence-time.

For $d_{dr} \gtrsim 60$ μm we see that the average residence-time increases with increasing drop-size. This is because the maximum droplet lateral-velocity decreases with increasing drop-size, see Section 5.3.4, resulting in an increase of the minimum residence-time, see Eq. (5). This is also visible in the top left graph of Fig. 8: for larger droplets the 'lower border' of the joint-pdf does not follow the dashed line with $t_{res} = 0.02$ s.

According to Lopes and Dukler (1986), and references therein, the droplet lateral-velocity is proportional to the friction velocity. Since the variation in $u_{\nabla p}$ between the measured flow conditions is rather small (about a factor 1.6), this can explain the small variation in the droplet residence-time (about a factor 2). However, since $u_{\nabla p,G21L1} < u_{\nabla p,G21L4}$, we expect $t_{res,G21L1} > t_{res,G21L4}$, whereas the opposite is observed. Moreover, we see a variation in $u_{\nabla p}$ for the churn-annular flows with u_{sl}, but the residence-time is more or less equal. The reason for this is not yet clear, but is probably strongly related to the droplet ejection phenomena at the interface, which we were unable to determine.

From Fig. 13 it is clear that the droplets with $d_{dr} \gtrsim 100$ μm have an average relaxation-time of the order of or larger than $\frac{1}{2}t_{res,dr}$. Therefore, these droplets are still accelerating at the center of the pipe, resulting in a large slip-velocity, see Section 5.3.

5.5. Dispersed-phase pressure-gradient

The dispersed-phase pressure-gradient is estimated using Eq. (9), i.e., directly from the PDA-measurements. However, we can only perform measurements for $|y| < 0.7R$, whereas in the region $0.7R < |y| < R$ the contribution to ∇p_{dr} may be significantly larger: closer to the interface the droplets that move away from the interface accelerate stronger. Here, the overall pressure-gradient, which is given in Table 3, is calculated as the average value for $|y| < 0.7R$.

In Fig. 14 the profile of ∇p_{dr} in the pipe cross-section is plotted, from which we observe that ∇p_{dr} is slightly core-peaking. This is probably caused by the droplet slip-velocity, since the droplet concentration and the drop-size are nearly constant over the cross-section. The product $C\, u_{z,s,dr}^2\, d_{32}^2$ is the most important factor in the dispersed-phase pressure-gradient; for G12L1 and G21L2 this product is almost equal, hence ∇p_{dr} is roughly equal. The differences are mainly due to the different drag-coefficient for the two flow-conditions.

The acceleration of the dispersion is characterised by: $a_{z,dr} \approx \bar{u}_{z,dr}/t_{res} \approx \nabla p_{dr}/(\rho_l \alpha_{dr})$, and is shown in Fig. 15, using ∇p_{dr} at the center of the pipe. From Fig. 15 it is clear that (i) the acceleration of the droplets is much more important than their weight, $a_{z,dr} \gg g$, (ii) droplets with a diameter $d_{dr} \approx 50$ μm accelerate strongest, resulting in the largest pressure-gradient per unit of holdup, and (iii) a smaller residence-time results in a larger mean acceleration, see also Fig. 13.
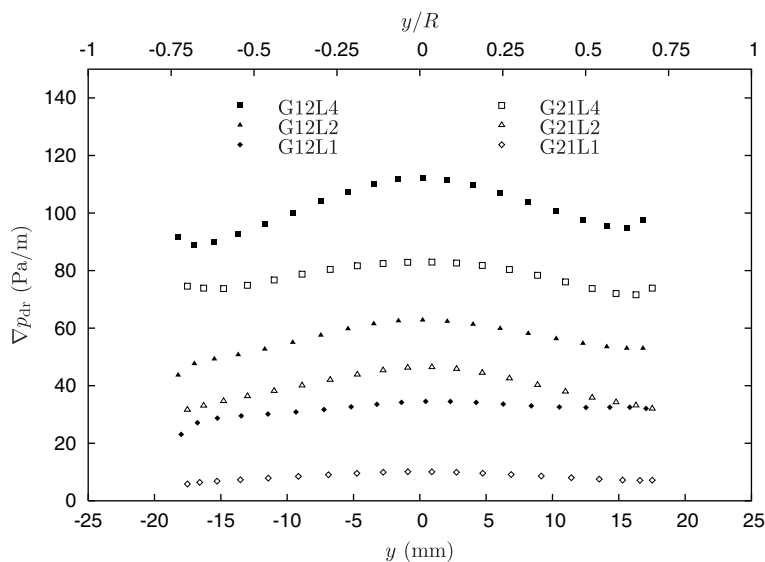

Fig. 14. Dispersed-phase pressure-gradient calculated with the direct method in the cross-section of the pipe.
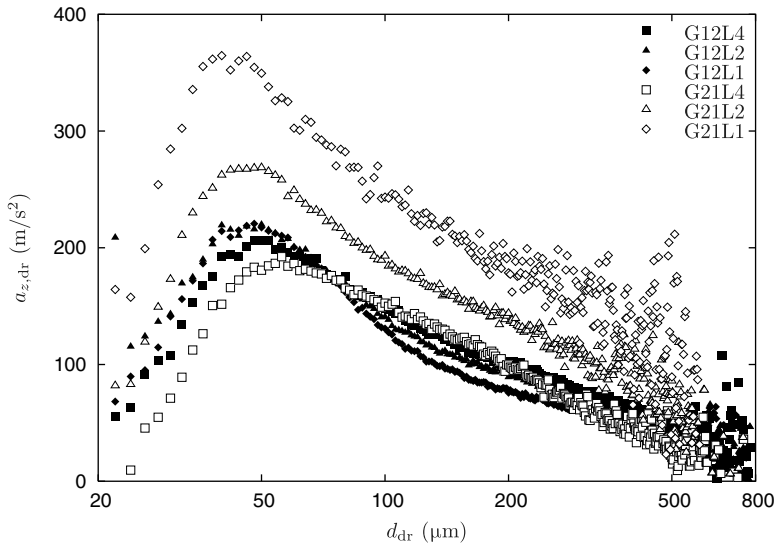
Fig. 15. Acceleration of droplets.

When we compare a churn-annular flow and a cocurrent annular flow with an equal holdup, and an equal acceleration, e.g., G12L2 and G21L4, we observe that ∇p_{dr} is larger for the cocurrent flow than for the churn-annular flow. Because the droplets in G21L4 are on average smaller than in G12L2, they accelerate stronger. Therefore, per unit of holdup, the dispersion of G21L4 can subtract energy more efficiently from the system than the dispersion of G12L2, resulting in a larger ∇p_{dr}.

Since the residence-time of tracer–droplets is relatively large, see Fig. 13, their mean acceleration is small (i.e., their contribution to the pressure-gradient ideally is zero).

5.6. Flow reversal

In Fig. 8 we observe that for G12L2 at $y = -0.7R$ almost all droplets move with an axial-velocity $u_{z,dr} \gtrsim 3$ m/s. When droplets would flow counter-current in the churn-annular flow, causing liquid down-flow as proposed by Turner et al. (1969), we can not measure them directly: due to the film extraction droplets are not created downstream of the PDA-detection volume. However, if Turners idea is true, we expect to find a large amount of droplets that move with an axial-velocity close to zero, and that these droplets are very large. Since only 0.4% of the dispersed-phase holdup is by droplets with an axial-velocity close to zero ($u_{z,dr} < 3$ m/s), and since their mean volume-diameter is about 200 μm, the idea that the droplets directly cause liquid loading is unlikely. Note that the maximum detected diameter of these slowest droplets is only about 350 μm, which is much smaller than 8.5 mm which is the droplet diameter that is supposed to cause down flow. Moreover, since it is expected that droplets are created with a maximum initial drop-diameter of the order of the film-thickness, coalescence should be very important in order to obtain such large drop sizes. This is not supported by Fig. 7, showing the free-path-length of the droplets.

The droplets may still affect the flow reversal, since they are expected to decrease the gas-phase velocity near the gas–liquid interface, and hence the interfacial shear. A decrease in the interfacial shear may lead to an instability of the liquid film.

For G21L4 an amount of 43% of the liquid flow rate is entrained, contributing about 10% of the total pressure-gradient. If we would have no entrainment, with equal gas and liquid flow rates, this would result in an increase of both the liquid film-thickness and the interfacial shear of about 20% (assuming a parabolic velocity profile in the liquid film, with no slip and zero shear at the pipe wall). Hence the total pressure gradient would be about 8% larger without entrainment. This suggests that for a given total pressure-gradient and liquid flow-rate in a cocurrent annular flow, the gas flow-rate is larger with entrainment than without it. The liquid

down-flow as caused by an instability of the liquid film will be delayed with increasing entrainment, since for a cocurrent annular flow the liquid film-thickness decreases with increasing entrainment.

However, once the film becomes unstable and film-churning is occurring we speculate that locally the transport of liquid in the film stalls, and liquid will accumulate, making the film-thickness very large and independent of the amount of entrainment. In such a case, the only effect of the dispersed-phase will be a decrease in the interfacial shear, increasing the liquid down flow.

6. Conclusion

In this paper we have investigated six vertical upward annular air–water pipe-flows in a 50 mm diameter pipe: three in the churn-annular regime with $u_{sg} = 12$ m/s, and three in the cocurrent annular regime with $u_{sg} = 21$ m/s. For both flow regimes the liquid flow-rates are set at $u_{sl} = 1$, 2 or 4 cm/s. We have used a PDA to measure the pdf of both drop-size and droplet-velocity at 15 locations in the pipe-cross-section. The total pressure-gradient, the amount of entrainment and the liquid down-flow are measured simultaneously. With the PDA-measurements we can make an estimate of the gas-phase mean velocity and velocity fluctuations and of the dispersed-phase drop-size, drop-velocity, concentration and pressure-gradient.

The gas-phase of a cocurrent annular flow, seems to behave similarly to a single-phase pipe-flow with a uniform wall-roughness. In contrast, the churn-annular flows show a rather uniform gas-phase velocity-fluctuation profile, the reason for this is not yet understood. For all flow conditions the gas-phase velocity-fluctuations scale roughly with the friction velocity.

For both the churn-annular flows and the cocurrent annular flows the drop-size distribution has an exponential decreasing tail, and a fall-off at the smallest drop-sizes. Breakup and coalescence seem not to be dominant processes in the core of the flow for the flow conditions we measured, and the drop-size distributions are determined by the atomisation process. Comparing with Fore and Dukler (1995a), we find a good agreement on the average dispersed-phase properties (R_A, δ_f, ∇p_{dr} and ∇p_{tot}) in the cocurrent annular flow for the smaller liquid flow-rates, $u_{sl} < 3$ cm/s. Using their model we have estimated the droplet residence-time from the PDA-data, which is an important parameter in predicting the dispersed-phase pressure-gradient.

Since the mean residence-time of the droplets is of the order of or smaller than the relaxation time for the droplets with $d_{dr} \gtrsim 100$ μm, these droplets are constantly accelerating, and their acceleration is much stronger than the gravitational acceleration. For the majority of the droplet-population, the slip-velocity is much larger than the terminal free-fall velocity in a stagnant medium. The dispersed-phase pressure-gradient is maximum about 10% of the total pressure-gradient for the flow conditions we have measured. We have not observed any droplet flowing counter-currently with the gas-flow, making the physical background of the Turner criterion for liquid loading implausible.

The presence of entrained liquid decreases the total pressure-gradient and the interfacial shear. Since an increase in entrainment decreases the liquid film-thickness in a cocurrent flow, the liquid film will be more stable. In a churn-annular flow the entrainment may not influence the liquid film-thickness, and the reduced interfacial shear increases the down-flow.

References

Albrecht, H.-E., Borys, M., Damaschke, N., Tropea, C., 2003. Laser Doppler and Phase Doppler Measurement Techniques. Springer-Verlag, Berlin Heidelberg.

Al-Sarkhi, A., Hanratty, T.J., 2002. Effect of pipe diameter on the drop size in a horizontal annular gas–liquid flow. Int. J. Multiphase Flow 28, 1617–1629.

Azzopardi, B.J., 1997. Drops in annular two-phase flow. Int. J. Multiphase Flow 23, 1–53, Supplementary.

Azzopardi, B.J., 1999. Turbulence modification in annular gas/liquid flow. Int. J. Multiphase Flow 25, 945–955.

Azzopardi, B.J., Hewitt, G.F., 1997. Maximum drop sizes in gas–liquid flows. Multiphase Sci. Technol. 9, 109–204.

Azzopardi, B.J., Teixeira, J.C.F., 1994. Detailed measurements of vertical annular two-phase flow – Part i: Drop velocities and sizes. J. Fluids Eng. 116, 792–795.

Azzopardi, B.J., Pierarcey, A., Jepson, D.M., 1991. Drop size measurements for annular two-phase flow in a 20 mm diameter vertical tube. Exp. Fluids 11, 191–197.

Fore, L.B., Dukler, A.E., 1995a. Droplet deposition and momentum transfer in annular flow. AIChE J. 41, 2040–2047.

Fore, L.B., Dukler, A.E., 1995b. The distribution of drop size and velocity in gas–liquid annular flow. Int. J. Multiphase Flow 21, 137–149.

Hay, K.J., Liu, Z.-C., Hanratty, T.J., 1998. A backlighted imaging technique for particle size measurements in two-phase flows. Exp. Fluids 25, 226–232.

Hetsroni, G., 1989. Particles–turbulence interaction. Int. J. Multiphase Flow 15, 735–746.

Hurlburt, E.T., Hanratty, T.J., 2002. Measurement of drop size in horizontal annular flow with the immersion method. Exp. Fluids 32, 692–699.

Kemp, H.K., 2004. Droplet size and velocity measurements in annular flow using phase-doppler anemometry. Master's thesis, Multi Scale Physics, Delft University of Technology.

Lopes, J.C.B., Dukler, A.E., 1986. Droplet entrainment in vertical annular flow and its contribution to momentum transfer. AIChE J. 32, 1500–1515.

Marmottant, P., Villermaux, E., 2004. On spray formation. J. Fluid Mech. 498, 73–111.

Mugele, R.A., Evans, H.D., 1951. Droplet size distribution in sprays. Ind. Eng. Chem. 43, 1317–1324.

Oudeman, P., 1989. Improved prediction of wet-gas-well performance (spe 19103), in: Proc. of SPE Gas Technology Symp., Dallas, USA.

Sekoguchi, K., Takeishi, M., 1989. Interfacial structures in upward huge wave flow and annular flow regimes. Int. J. Multiphase Flow 15, 295–305.

Simmons, M.J.H., Hanratty, T.J., 2001. Droplet size measurements in horizontal annular gas–liquid flow. Int. J. Multiphase Flow 27, 861–883.

Tsuji, Y., Morikawa, Y., Shiomi, H., 1984. LDV measurements of an air-solid two phase flow in a vertical pipe. J. Fluid Mech. 139, 417–434.

Turner, R.G., Hubbard, M.G., Dukler, A.E., 1969. Analysis and prediction of minimum flow rate for the continuous removal of liquid from gas wells. J. Petrol. Technol., 1475–1482.

Wallis, G.B., 1969. One Dimensional Two-Phase Flow. McGraw-Hill.

Westende, J.M.C., van 't., Belt, R.J., Portela, L.M., Mudde, R.F., Oliemans, R.V.A., 2004. Interaction of particles with secondary flow in high reynolds number horizontal pipe flow, in: Proc. of 3rd Int. Symp. on Two-Phase Modelling and Exp., Pisa, Italy. ISBN 88-467-1075-4.

Westende, J.M.C., van 't., Belt, R.J., Portela, L.M., Mudde, R.F., Oliemans, R.V.A., 2005. Droplet characterisation in upward annular dispersed pipe flow, in: Proc. of 11th Workshop on Two-Phase Flow Predictions, Merseburg, Germany. ISBN 3-86010-767-4.

Zabaras, G., Dukler, A.E., Moalem-Maron, D., 1986. Vertical upward cocuurent gas–liquid annular flow. AIChE J. 32, 743–829.

Zaidi, S.H., Altunbas, A., Azzopardi, B.J., 1998. A comparative study of phase doppler and laser diffraction techniques to investigate drop sizes in annular two-phase flow. Chem. Eng. J. 71, 135–143.